Journal of Zhejiang University-SCIENCE A (Applied Physics & Engineering) 2023 24(8):653-672
www.jzus.zju.edu.cn; www.springer.com/journal/11582
E-mail: jzus_a@zju.edu.cn

Research Article

https://doi.org/10.1631/jzus.A2200578

Vibration suppression of composite panel with variable angle tow design and inerter-based nonlinear energy sink

Chen ZHOU[1,2], Jian YANG[2,3]✉, Yingdan ZHU[1,4]✉, Chendi ZHU[5]

[1]*Zhejiang Provincial Key Laboratory of Robotics and Intelligent Manufacturing Equipment Technology, Ningbo Institute of Material Technology & Engineering, Chinese Academy of Sciences, Ningbo 315201, China*
[2]*Department of Mechanical, Materials and Manufacturing Engineering, University of Nottingham Ningbo China, Ningbo 315100, China*
[3]*International Academy of Marine Economy and Technology (IAMET), University of Nottingham Ningbo China, Ningbo 315100, China*
[4]*Center of Materials Science and Optoelectronics Engineering, University of Chinese Academy of Sciences, Beijing 100049, China*
[5]*Ningbo Institute of Dalian University of Technology, Ningbo 315016, China*

Abstract: This study investigates the vibration transmission and suppression of a laminated composite panel with variable angle tow (VAT) designs and an attached inerter-based passive nonlinear energy sink. Based on analytical and numerical methodologies, the substructure technique is used to obtain a steady-state dynamic response and the results are verified by experimental and analytical methods. It is demonstrated that fiber orientation has a significant impact on the natural frequencies. The dynamic responses and energy transmission path characteristics are determined and evaluated by forced vibration analysis. The main vibration transmission paths inside the structure are displayed using power flow density vectors. It is demonstrated that the dynamic responses of the plate can be changed considerably by using various fiber placement schemes and passive suppression devices. In addition, it is indicated that the vibration transmission paths are significantly influenced by the tailored fiber angles for improved dynamic performance. Our investigation enhances the understanding of enhanced vibration suppression designs of variable-stiffness composite plates with attached passive devices.

Key words: Laminated composite plate; Variable stiffness; Substructure method; Passive device; Power flow analysis

1 Introduction

Composite materials are becoming increasingly important in modern engineering with applications in aerospace, automotive, and underwater structures (Cho et al., 2015). Materials in this category are made by the blending of two or more components with performance advantages in the obtained mixture compared to the original individual materials. Compared with conventional metal structures, composite structures exhibit superior performance in areas such as specific strength, stiffness, fatigue resistance, and corrosion resistance. Good designability is another significant advantage of composite structures (Zuo et al., 2015). With the ongoing improvement of fiber laying equipment, the laying of fibers with changing angles has become possible (Gurdal and Olmedo, 1993; Wu et al., 2012). Variable angle tow (VAT) fiber reinforced composites have spatially non-constant stiffness characteristics, allowing the stiffness of each point to be designed according to the loading direction path (Nik et al., 2014b; Jahangir et al., 2022). In this way, the overall load capacity of the structure and the material use efficiency can be significantly improved (Lopes et al., 2007; Rahman et al., 2011; White et al., 2014, 2015). However, the design space is enlarged when using VAT designs, and the total number of design variables becomes large, bringing challenges for effective design and analysis (Pedersen, 1991; Setoodeh et al., 2005). More recently, several mechanical properties of VAT plates have been studied, such as the compressive (Vijayachandran and Waas, 2022b), buckling (Coburn et al., 2014; Raju et al., 2015), and postbuckling (Wu et al., 2013, 2018)

✉ Jian YANG, jian.yang@nottingham.edu.cn
Yingdan ZHU, y.zhu@nimte.ac.cn
Jian YANG, https://orcid.org/0000-0003-4255-9622
Chendi ZHU, https://orcid.org/0000-0003-1156-3557

Received Dec. 2, 2022; Revision accepted Apr. 10, 2023; Crosschecked July 19, 2023

properties. Furthermore, the influence of some defects such as gaps and overlaps in the manufacturing of VAT plate has been studied (Nik et al., 2014a; Akbarzadeh et al., 2016; Vijayachandran and Waas, 2022a).

Composite laminates in engineering applications are often subjected to dynamic loading, therefore it is crucial to understand their vibrational properties to avoid structural resonance and to ensure the safety of the application. Several studies have analyzed the vibration characteristics of composite laminates with straight fibers (Zhu and Yang, 2019). In terms of vibration suppression, reducing the net power transmission to the structure of interest and minimizing the power flow within the structure are the two primary objectives. To describe the dynamic response of vibrating systems, force and velocity were combined into a single variable according to the vibration power flow concept (Zhu et al., 2021a; Zhu and Yang, 2022). To examine various linear systems and structures, a range of power flow analysis (PFA) methods have been employed (Mace and Shorter, 2000; Xiong et al., 2001). The PFA approach was created recently to assess the frequency of the Duffing oscillator (Yang et al., 2014) and was used to evaluate the effectiveness of nonlinear vibration isolators and absorbers (Yang et al., 2013, 2015, 2016) in terms of the flow and transmission of vibrational energy. In addition, PFA was applied to the quantitative analysis of vibration transfer between an interactive oscillator with a coupled nonlinear interface (Shi et al., 2019) and coupled nonlinear oscillation systems (Shi and Yang, 2020). Recently, the vibration transfers of non-smooth systems such as impact oscillators and frictional systems have also been investigated (Dai et al., 2020, 2022).

For VAT composite structures, the required vibration analysis methods are usually more complex than those for structures with constant stiffness. The free vibration of VAT composite laminates has been studied (Houmat, 2013). Investigations were conducted on the frequencies of a conical shell with variable stiffness (Wu and Lee, 2001; Blom et al., 2008). The Ritz method and spline function were used to estimate the natural frequencies of a plate with curved fibers and these two methods were shown to significantly speed up calculation times compared to the finite element approach (Honda et al., 2008). Using lamination characteristics to parameterize the modification of the stiffness properties, the maximization of the fundamental frequency of VAT composite panels has been targeted (Abdalla et al., 2007). The vibration characteristics of VAT composite annular thin plates were revealed using the weighted residuals approach and the natural frequency was shown to be impacted by the elastically restrained edges, as well as by material and geometrical factors (Tan and Nie, 2016). Importantly, the experimental vibration testing of composite laminates is necessary for validation of the analytical and numerical results. However, very few studies have focused on forced vibration analysis, particularly on vibration power flow analysis of VAT composite plates.

Besides the tailoring of fiber orientation, another way to improve the vibration performances of engineering composite structures is to add passive vibration suppression devices (Zhu et al., 2021b). Passive devices consisting of spring and dampers are widely used in vibration engineering. For instance, a two-terminal device called an inerter has been proposed, with an applied force proportional to the relative velocities of its terminals (Smith and Wang, 2004). Inerters have been shown to provide excellent suppression performance in different engineering designs (Wang et al., 2010; Lazar et al., 2014; Zhang et al., 2017), in landing gears for shimmy vibration reduction (Li et al., 2017), and in railway and vehicle suspension systems (Wang et al., 2009; Jiang et al., 2012). Passive vibration isolators have been extensively studied and utilized to reduce excessive vibration transmission. Much research on passive vibration control systems has concentrated on spring and damper parameter optimization. For example, the spring and damping coefficients were chosen for a dynamic vibration absorber to achieve a lower peak response (Rivin, 2003; Ibrahim, 2008). Nonlinear energy sinks (NES) equipped with an inerter can perform better compared to conventional NES by having much lower physical mass (Javidialesaadi and Wierschem, 2019). The NES was proposed to eliminate multimode resonances in composite plates (Chen et al., 2020). However, there has been very limited research on the design and analysis of a variable fiber angle and inerter-based passive device for the vibration suppression of composite structures. Furthermore, the efficient use of the PFA approach for the effective design and tailoring of vibration transmission paths using VAT design and passive device needs further exploration.

This study examines the vibration transmission characteristics of a laminated composite plate and the

vibration suppression effect when using a variable-stiffness design and inerter-based devices. In addition, the impact of fiber orientations on the natural frequencies and the displacement, kinetic energy response, and energy transmission path (ETP) for harmonically forced VAT composite structures are analyzed. The discussion also includes the impacts of the inerter-based suppression device. The remaining information in this paper is organized as follows: The model description of the VAT composite plate and passive device is provided in Section 2. The substructure analytical technique applied to obtain the dynamic response is demonstrated in Section 3. The power flow analysis and related formulations of the variables of time-averaged power flow are presented in Section 4. The results and discussion associated with the relationships between the various structural parameters and vibration transmission properties of the two different configurations of VAT plates are presented in Section 5. Finally, conclusions are drawn.

2 Mathematical modelling

2.1 Model description

Fig. 1a presents a schematic diagram of a rectangular laminated composite plate with an attached passive NES vibration suppression device. The plate is designed with length L, width W, and thickness h in the directions of OX, OY, and OZ, respectively. A set of orthogonal axes called $OXYZ$ is created in a global Cartesian coordinate system. A vertical external excitation force $F=\tilde{f}_e e^{i\omega t}$ is applied to the point A (x_e, y_e), and four edges of the plate are all simply supported, where $\tilde{f}_e$, ω, and t are the complex amplitude, frequency, and time

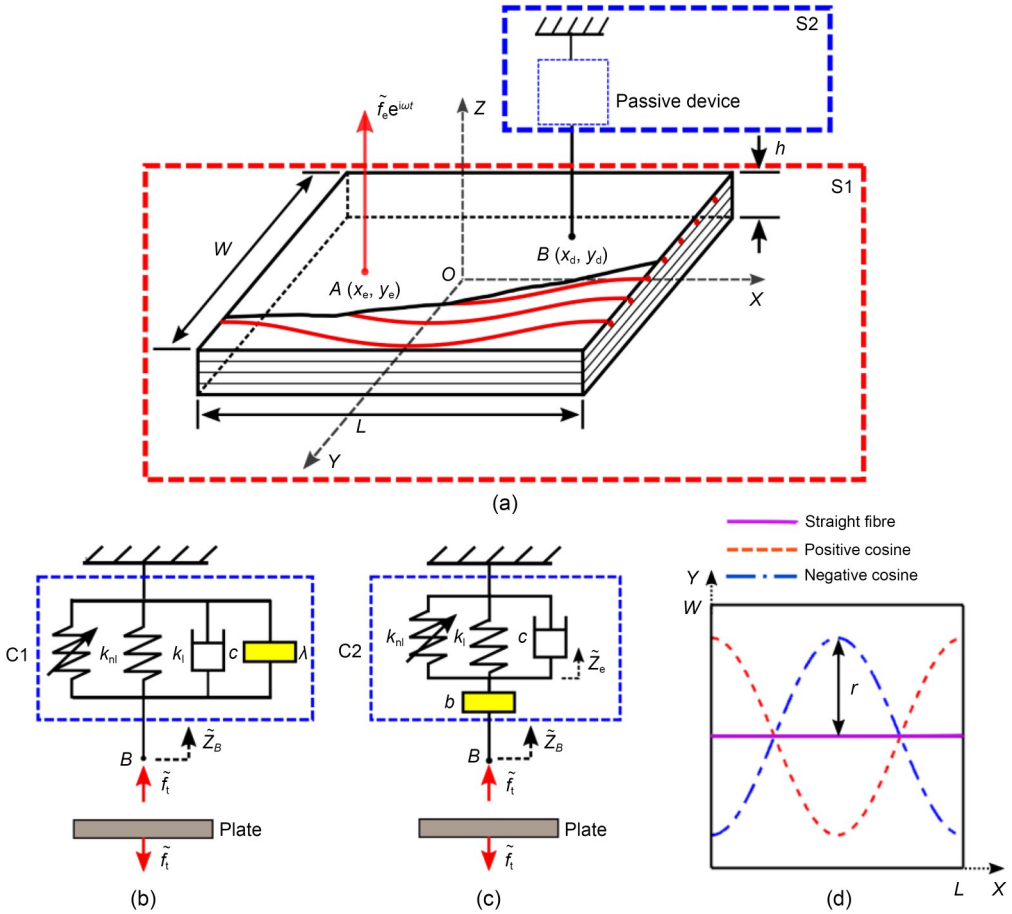

Fig. 1 (a) Schematic diagram of a VAT composite plate with an inerter-based passive NES device attached; (b) NES configuration C1 (the spring, damper, and inerter are set in parallel); (c) NES configuration C2 (the spring and damper are initially set up in parallel and then linked in series with an inerter); (d) Different fiber angle functions. Reference to color refers to the online version of this figure. Explanations of variables will be given in the following sections

of the applied force, respectively. Two different kinds of the inerter-based passive NES devices C1 and C2 are presented in Figs. 1b and 1c, respectively, and the coefficients of each element are set as k_1 for the linear spring, k_{nl} for the nonlinear spring, c for the viscous damper, and λ for the inerter. It is assumed that the inertance of the inerter is much larger than its physical mass, which can therefore be neglected in the analysis.

Fig. 1d presents different fiber orientations comprising straight fiber cases shown by the solid line. The fiber placed is curved in red and blue lines; to allow the stiffness of the plate to change continuously, the function of the blue one is as described as

$$f(x)=y=r\cdot\cos\left(\frac{2\pi x}{l}\right), \tag{1}$$

where r denotes half of the amplitude, and l is the wavelength of this periodic function. It is noted that, using Eq. (1), only the direction of a single fiber-tow is considered, and no consideration is included for manufacturing constraints and defects such as gaps and overlaps. Thus, the variable fiber orientation angle $\theta(x)$ can be obtained by taking the first derivative of $f(x)$ against x:

$$\frac{\mathrm{d}f}{\mathrm{d}x}=-\frac{2\pi r}{l}\sin\left(\frac{2\pi x}{l}\right)=\tan(\theta(x)), \tag{2}$$

$$\theta(x)=\arctan\left[-\frac{2\pi r}{l}\sin\left(\frac{2\pi x}{l}\right)\right]. \tag{3}$$

The first configuration (i.e., scheme M0) is for the laminated plate for which the fiber angle for every layer is set the same. The second configuration (i.e., scheme M1 with [+ + + +]) is for laminated plates with variable stiffness with fiber angle in each layer described by the same function expressed by Eq. (1). In the third configuration (i.e., scheme M2 with [+ − + −]), the plate is symmetric about the *OX*-*OY* plane. The fiber angles of the odd layers are described by Eq. (1) while those of the even layers are described by

$$f(x)=y=-r\cdot\cos\left(\frac{2\pi x}{l}\right). \tag{4}$$

Note that the coordinate systems used for the main material and the entire connected structure may not match. Several fiber angles can also be set for different layers of composite laminates. As a consequence, the connections between stresses and strains in one coordinate system and their equivalent values in another must be determined.

The constitutive equations of each layer are expressed as (Reddy, 1997)

$$\begin{Bmatrix}\sigma_1\\ \sigma_2\\ \tau_{12}\end{Bmatrix}=\begin{bmatrix}Q_{11} & Q_{12} & 0\\ Q_{12} & Q_{22} & 0\\ 0 & 0 & Q_{66}\end{bmatrix}\begin{Bmatrix}\varepsilon_1\\ \varepsilon_2\\ \gamma_{12}\end{Bmatrix}, \tag{5a}$$

$$\begin{Bmatrix}\tau_{23}\\ \tau_{13}\end{Bmatrix}=\begin{bmatrix}Q_{44} & 0\\ 0 & Q_{55}\end{bmatrix}\begin{Bmatrix}\gamma_{23}\\ \gamma_{13}\end{Bmatrix}, \tag{5b}$$

where σ and τ represent the normal and shear stresses, respectively; ε and γ represent the normal and shear strains, respectively; Q_{ij} represent the plane stress-reduced stiffnesses, which are related to the engineering constants according to

$$Q_{11}=\frac{E_1}{1-\nu_{12}\nu_{21}},\ Q_{12}=\frac{\nu_{12}E_2}{1-\nu_{12}\nu_{21}},\ Q_{22}=\frac{E_2}{1-\nu_{12}\nu_{21}}, \tag{6a}$$

$$Q_{66}=G_{12},\ Q_{44}=G_{23},\ Q_{55}=G_{13},\ G_{12}=G_{13}, \tag{6b}$$

where E is Young's modulus, G is the shear modulus, and ν is Poisson's ratio.

For an orthotropic material, the stress–strain relation involving the plane stress assumption is given by

$$\begin{Bmatrix}\sigma_{xx}\\ \sigma_{yy}\\ \tau_{xy}\end{Bmatrix}=\begin{bmatrix}\bar{Q}_{11} & \bar{Q}_{12} & \bar{Q}_{16}\\ \bar{Q}_{12} & \bar{Q}_{22} & \bar{Q}_{26}\\ \bar{Q}_{16} & \bar{Q}_{26} & \bar{Q}_{66}\end{bmatrix}\begin{Bmatrix}\varepsilon_{xx}\\ \varepsilon_{yy}\\ \gamma_{xy}\end{Bmatrix}, \tag{7}$$

where

$$\begin{aligned}
\bar{Q}_{11}&=Q_{11}\cos^4\theta+2(Q_{12}+2Q_{66})\sin^2\theta\cdot\cos^2\theta+Q_{22}\sin^4\theta,\\
\bar{Q}_{12}&=(Q_{11}+Q_{22}-4Q_{66})\sin^2\theta\cdot\cos^2\theta+Q_{12}(\sin^4\theta+\cos^4\theta),\\
\bar{Q}_{22}&=Q_{11}\sin^4\theta+2(Q_{12}+2Q_{66})\sin^2\theta\cdot\cos^2\theta+Q_{22}\cos^4\theta,\\
\bar{Q}_{16}&=(Q_{11}-Q_{22}-2Q_{66})\sin\theta\cdot\cos^3\theta+\\
&\quad(Q_{12}-Q_{22}+2Q_{66})\sin^3\theta\cos\theta,\\
\bar{Q}_{26}&=(Q_{11}-Q_{22}-2Q_{66})\sin^3\theta\cos\theta+\\
&\quad(Q_{12}-Q_{22}+2Q_{66})\sin\theta\cdot\cos^3\theta,\\
\bar{Q}_{66}&=(Q_{11}+Q_{22}-2Q_{12}-2Q_{66})\sin^2\theta\cdot\cos^2\theta+\\
&\quad Q_{66}(\sin^4\theta+\cos^4\theta).
\end{aligned} \tag{8}$$

Note that the constitutive relation is for a single lamina in global coordinates.

In the first-order shear deformation theory (FSDT), the displacements for a certain point on the plate are

represented by the letters u, v, and w, respectively, in the directions of OX, OY, and OZ.

$$u(x,y,z,t)=u_0(x,y,t)+z\phi_x(x,y,t), \tag{9a}$$
$$v(x,y,z,t)=v_0(x,y,t)+z\phi_y(x,y,t), \tag{9b}$$
$$w(x,y,z,t)=w_0(x,y,t), \tag{9c}$$

where ϕ_x and ϕ_y denote rotations around the OY and OX axes, respectively. (u_0, v_0, w_0) are the displacement components along the (x, y, z) coordinate directions, respectively, of a point on the midplane.

The relationship between the internal forces N or moments M and the displacements is:

$$\begin{Bmatrix} N_{xx} \\ N_{yy} \\ N_{xy} \\ M_{xx} \\ M_{yy} \\ M_{xy} \end{Bmatrix} = \begin{bmatrix} A_{11} & A_{12} & A_{16} & B_{11} & B_{12} & B_{16} \\ A_{12} & A_{22} & A_{26} & B_{12} & B_{22} & B_{26} \\ A_{16} & A_{26} & A_{66} & B_{16} & B_{26} & B_{66} \\ B_{11} & B_{12} & B_{16} & D_{11} & D_{12} & D_{16} \\ B_{12} & B_{22} & B_{26} & D_{12} & D_{22} & D_{26} \\ B_{16} & B_{26} & B_{66} & D_{16} & D_{26} & D_{66} \end{bmatrix} \times \begin{bmatrix} \dfrac{\partial u_0}{\partial x}+\dfrac{1}{2}\left(\dfrac{\partial w_0}{\partial x}\right)^2 \\ \dfrac{\partial v_0}{\partial y}+\dfrac{1}{2}\left(\dfrac{\partial w_0}{\partial y}\right)^2 \\ \dfrac{\partial u_0}{\partial y}+\dfrac{\partial v_0}{\partial x}+\dfrac{\partial w_0}{\partial x}\dfrac{\partial w_0}{\partial y} \\ \dfrac{\partial \phi_x}{\partial x} \\ \dfrac{\partial \phi_y}{\partial y} \\ \dfrac{\partial \phi_x}{\partial y}+\dfrac{\partial \phi_y}{\partial x} \end{bmatrix}, \tag{10}$$

$$\begin{Bmatrix} N_{yz} \\ N_{xz} \end{Bmatrix} = K\begin{bmatrix} A_{44} & A_{45} \\ A_{45} & A_{55} \end{bmatrix}\begin{Bmatrix} \dfrac{\partial w_0}{\partial y}+\phi_y \\ \dfrac{\partial w_0}{\partial x}+\phi_x \end{Bmatrix}, \tag{11}$$

where K is the shear correction factor, given as K=5/6. A_{ij}, D_{ij}, and B_{ij} denote the extensional, bending, and bending-extensional coupling stiffnesses, respectively, which are related to the lamina stiffnesses $\bar{Q}_{ij}^{(k)}$ by

$$\left(A_{ij},B_{ij},D_{ij}\right)=\int_{-\frac{h}{2}}^{\frac{h}{2}}\bar{Q}_{ij}(1,z,z^2)\,\mathrm{d}z=\sum_{k=1}^{N}\int_{z_k}^{z_{k+1}}\bar{Q}_{ij}^{(k)}(1,z,z^2)\,\mathrm{d}z. \tag{12}$$

2.2 Inerter-based NES device

Two kinds of passive devices are presented in Figs. 1b and 1c. For configuration C1, the spring, damper, and inerter are set in parallel. In contrast, in configuration C2, the spring and damper are initially set up in parallel and then linked in series through an inerter. Linear and nonlinear springs are considered and investigated in both configurations. The displacement of the attachment point B in the OZ direction is denoted by $\tilde{Z}_B$. The passive device is subjected to a harmonic force $\tilde{f}_t$ by the plate. When C1 contains only the linear spring, this can be expressed as

$$\tilde{f}_t=k_1\tilde{Z}_B+c\dot{\tilde{Z}}_B+\lambda\ddot{\tilde{Z}}_B=(k_1-\lambda\omega^2+\mathrm{i}\omega c)\,\tilde{Z}_B. \tag{13}$$

On the other hand, when C1 is with a purely nonlinear spring representing a nonlinear energy sink, we have:

$$\tilde{f}_t=k_{nl}\tilde{Z}_B^3+c\dot{\tilde{Z}}_B+\lambda\ddot{\tilde{Z}}_B. \tag{14}$$

For configuration C2, when it contains only the linear spring, it follows that:

$$\tilde{f}_t=k_1\tilde{Z}_e+c\dot{\tilde{Z}}_e=(k_1+\mathrm{i}\omega c)\,\tilde{Z}_e=\lambda\left(\ddot{\tilde{Z}}_B-\ddot{\tilde{Z}}_e\right)=-\lambda\omega^2\left(\tilde{Z}_B-\tilde{Z}_e\right), \tag{15}$$

where $\tilde{Z}_e$ represents the upper terminal of the complex displacement amplitude of the inerter. By cancelling out $\tilde{Z}_e$ in Eq. (15), we can obtain:

$$\tilde{f}_t=\frac{\lambda\omega^2(k_1+\mathrm{i}\omega c)}{\lambda\omega^2-(k_1+\mathrm{i}\omega c)}\tilde{Z}_B. \tag{16}$$

The equation governing the dynamics of configuration C2 with a purely nonlinear spring representing a nonlinear energy sink is:

$$\tilde{f}_t=k_{nl}\tilde{Z}_B^3+c\dot{\tilde{Z}}_e=\lambda\left(\ddot{\tilde{Z}}_B-\ddot{\tilde{Z}}_e\right). \tag{17}$$

3 Dynamic analysis using the substructure method

The substructure technique is used in this work to calculate the steady-state response of the integrated

system. For complex structures, obtaining comprehensive analytical solutions for the dynamic response is challenging, while the substructure method can deal with these problems at a low cost (Wang et al., 2002). In this method, the entire system is initially divided into various substructures. Then the vibration properties of the whole structure can be obtained by force balance and the continuity of displacement. Currently, when using the substructure method, the composite plate is subsystem I (S1), and the suppression device is subsystem II (S2) of the system.

3.1 Analysis of the composite plate

The receptance frequency response function is defined as the ratio between the complex amplitude (i.e., $\tilde{w}$) of the displacement of a point of interest (x_r, y_r) to that (i.e., $\tilde{f}_e$) of a concentrated harmonic force supplied at (x_e, y_e):

$$\tilde{\beta}_{re}=\frac{\tilde{w}(x_r,y_r)}{\tilde{f}_e(x_e,y_e)}. \tag{18}$$

For the plate structure, the receptance function can be written as:

$$\tilde{\beta}_{re}=\frac{4}{LW\mu}\sum_{m=1}^{\infty}\sum_{n=1}^{\infty}\frac{\varphi_{mn}(x_e,y_e)\,\varphi_{mn}(x_r,y_r)}{\omega_{mn}^2(1+\mathrm{i}\eta)-\omega^2}, \tag{19}$$

where m and n are used to indicate mode numbers, $\mu=\rho h$ is the mass per unit area, ρ is the density, η stands for the structural damping, and the mode shape function is represented by φ_{mn}. Note that as a plate is a continuous structure with an infinite number of modes, the modal sum will need to be truncated by varying m and n from 1 to fixed values. This is reasonable; high-order modes associated with high natural frequencies will have small contribution to the response.

3.2 Solution based on harmonic balance (HB) method

Two forces are applied to the simply supported plate. One is the external excitation force $\tilde{f}_e$ at point A and the other is $\tilde{f}_t$ provided by the NES suppression device located at point B. The displacement response amplitude at point B due to the force $\tilde{f}_e$ applied at point A is:

$$\tilde{z}_{Be}=\tilde{\beta}_{BA}\tilde{f}_e, \tag{20}$$

where

$$\tilde{\beta}_{BA}=\frac{4}{LW\mu}\sum_{m=1}^{\infty}\sum_{n=1}^{\infty}\frac{\varphi_{mn}(x_A,y_A)\,\varphi_{mn}(x_B,y_B)}{\omega_{mn}^2(1+\mathrm{i}\eta)-\omega^2}, \tag{21}$$

is the receptance function obtained from Eq. (19) by replacing the subscripts e and r with A and B, respectively. Similarly, the displacement response at point B due to a harmonic force with complex amplitude $\tilde{f}_t$ and frequency ω applied at point B is expressed by

$$\tilde{z}_{Bt}=\tilde{z}_{Be}=-\tilde{\beta}_{BB}\tilde{f}_t, \tag{22}$$

where

$$\tilde{\beta}_{BB}=\frac{4}{LW\mu}\sum_{m=1}^{\infty}\sum_{n=1}^{\infty}\frac{\varphi_{mn}(x_B,y_B)\,\varphi_{mn}(x_B,y_B)}{\omega_{mn}^2(1+\mathrm{i}\eta)-\omega^2}, \tag{23}$$

is the receptance function obtained from Eq. (19) by replacing the subscripts e and r both with B. Note that the negative sign in Eq. (22) is due to the direction of $\tilde{f}_t$ being opposite to the positive direction of the displacement in the vertical direction.

Therefore, the combined displacement response of point B, with contributions from $\tilde{f}_e$ and $\tilde{f}_t$ both with the same frequency ω, is expressed by

$$\tilde{z}_B=\tilde{z}_{Be}+\tilde{z}_{Bt}=\tilde{\beta}_{BA}\tilde{f}_e-\tilde{\beta}_{BB}\tilde{f}_t. \tag{24}$$

For the configuration C1 without k_{nl}, the unknown displacement $\tilde{z}_B$ and force $\tilde{f}_t$ can be obtained by solving Eqs. (13) and (24):

$$\tilde{z}_B=\frac{\tilde{\beta}_{BA}\tilde{f}_e}{1+(k_1-\lambda\omega^2+\mathrm{i}\omega c)\,\tilde{\beta}_{BB}}, \tag{25a}$$

$$\tilde{f}_t=\frac{(k_1-\lambda\omega^2+\mathrm{i}\omega c)\,\tilde{\beta}_{BA}\tilde{f}_e}{1+(k_1-\lambda\omega^2+\mathrm{i}\omega c)\,\tilde{\beta}_{BB}}. \tag{25b}$$

Similarly, for the configuration C2 without k_{nl}, the unknown $\tilde{z}_B$ and $\tilde{f}_t$ can be obtained by solving Eqs. (16) and (24):

$$\tilde{z}_B=\frac{(-k_1+\lambda\omega^2-\mathrm{i}\omega c)\,\tilde{\beta}_{BA}\tilde{f}_e}{\lambda\omega^2-(k_1+\mathrm{i}\omega c)+\lambda\omega^2(k_1+\mathrm{i}\omega c)\,\tilde{\beta}_{BB}}, \tag{26a}$$

$$\tilde{f}_t=\frac{\lambda\omega^2(k_1+\mathrm{i}\omega c)\,\tilde{\beta}_{BA}\tilde{f}_e}{\lambda\omega^2-(k_1+\mathrm{i}\omega c)+\lambda\omega^2(k_1+\mathrm{i}\omega c)\,\tilde{\beta}_{BB}}. \tag{26b}$$

When the suppression devices are with both linear and nonlinear springs, the HB method is used to obtain the dynamic response by approximating the unknown displacement $\tilde{z}_B e^{i\omega t}$ and transmitted force f_{Bt} as

$$\tilde{z}_B e^{i\omega t} = \sum_{q=1}^{U} \tilde{z}_{B,q} e^{iq\omega t}, \tag{27a}$$

$$f_{Bt} = \sum_{q=1}^{U} \tilde{f}_{t,q} e^{iq\omega t}, \tag{27b}$$

where $\tilde{z}_{B,q}$ and $\tilde{f}_{t,q}$ are the complex coefficients of the harmonic terms, and U is set as 1 when a first-order approximation is sought. Note that when using complex notations for the variables, only the real part carries physical meaning for the corresponding quantities. Eqs. (14) and (17) are used to establish the relationship between the complex amplitudes $\tilde{z}_{B,q}$ and $\tilde{f}_{t,q}$. Then the substructure method is used for the determination of the solution.

4 Energy-based performance index

In engineering structure design, to measure the vibration level of a structure, kinetic energy is a crucial factor (Xiong et al., 2003). At present, the maximum kinetic energy of composite plates is defined as

$$K_p = \frac{1}{2} \int_{y=0}^{y=W} \int_{x=0}^{x=L} \rho h V^2(x,y) \, dx dy, \tag{28}$$

where V is the velocity.

The laminated plate is subjected to a point excitation in the OZ direction and its kinetic energy is only measured in the direction of vertical motion. After completing the integration, the kinetic energy can be obtained by

$$K_p = \frac{2\omega^2}{LW\mu} \left| \sum_{m=1}^{\infty} \sum_{n=1}^{\infty} \frac{f_e \varphi_{mn}}{\omega_{mn}^2 (1+i\eta) - \omega^2} \right|^2. \tag{29}$$

The design of a composite plate requires better vibration control which means that, under the excitation force, the kinetic energy level should be as low as possible.

Based on the definition of instantaneous power flow density vector (PFDV), its time-averaged quantity over a period of excitation T can be derived that:

$$\langle q_k \rangle = \frac{1}{T} \sum_{0}^{T} q_k dt = -\frac{1}{2} \mathrm{Re}\left\{ \sigma_{jk} v_j^* \right\}, \tag{30}$$

where q_k is the instantaneous power flow density vector, v_j^* is the velocity vector, and σ_{jk} is the stress tensor, with j, k=1, 2, 3.

Then, the two parts of the PFDVs are introduced with a time-averaged quantity:

$$\langle q_x \rangle = -\frac{1}{2} \mathrm{Re}\left\{ N_{xz} v^* + N_{xy} \dot{w}_y^* + N_{xx} \dot{w}_x^* - M_{xy} \dot{\theta}_x^* - M_{xx} \dot{\theta}_y^* \right\}, \tag{31a}$$

$$\langle q_y \rangle = -\frac{1}{2} \mathrm{Re}\left\{ N_{yz} v^* + N_{xy} \dot{w}_x^* + N_{yy} \dot{w}_y^* - M_{xy} \dot{\theta}_x^* - M_{yy} \dot{\theta}_x^* \right\}, \tag{31b}$$

where $\dot{w}^*$ and v^* represent complex conjugates of the displacements, and $\dot{\theta}^*$ represents the complex conjugate of the rotations.

5 Results and discussion

5.1 Experimental verification and free vibration

To validate the numerical results, experimental testing was carried out to determine the natural frequencies of the structure. Constant-stiffness and VAT carbon fiber/epoxy composite plates were fabricated using the vacuum-assisted resin injection (VARI) method. The fiber used was T700SC-12000, produced by Toray with a tensile modulus of 230 GPa. The resin was 4330A1B1 made by Epotech, with a modulus of 2.9 GPa. Two unidirectional carbon fiber/epoxy constant stiffness composite plates with fiber angles of 0° and 90° were manufactured by stacking and consolidating individual prepreg sheets. For the VAT composite plate, VAT machines form the braided fabric by stitching the fiber bunches on the unidirectional fabric with the desired function shape. Four pieces of braided fabric are stacked together, and one piece of unidirectional fabric is then placed on top to ensure a smooth surface of the final product. After that, they are placed under vacuum in an autoclave and pressurized during the heated cure cycle. Finally, after the sample is cured, it is cut into a rectangular shape with a dimension of 500 mm×50 mm with a water jet. It is noted that the method is not using prepregs and focusing on the fiber angle being steered using a machine for dry fibers and then the resin is injected unlike the automated tap layer. Therefore,

the manufacturing constraints do not include tape width, minimum radius, and creation of gaps and overlaps (Nik et al., 2014a; Akbarzadeh et al., 2016; Vijayachandran and Waas, 2022a).

After the fabrication step, modal tests were performed on samples to obtain their natural frequencies. Fig. 2 shows the hammer test configuration for a cantilever composite plate. The specific point of the structure was excited, and the force applied was measured by a force transducer installed inside the hammer. A light micro-accelerometer was placed at the centre of the outer edge of the sample to measure the data response of the plate. In addition, the accelerometer and the test sample were connected using adhesive glue to reduce the possible mass loading effect. Then, the measurement data were collected and processed by a Data Physics data acquisition instrument. The vibration response data were processed more than 10 times to ensure that the results were statistically representative.

The plate structure was divided into 181 elements in the finite element modeling (FEM) step, with each node having six degrees of freedom. A PC with Windows 10 operating system was used to do the calculations. The computer featured 16 GB RAM and an Intel Core i7-8750 processor of 2.2 GHz. With the properties measured by the samples and the damping ratio set as 0.01, the natural frequencies of structures could be determined.

The natural frequencies for two kinds of constant stiffness plates are compared in Table 1 using two different approaches. The error is defined as $\left(|f_1-f_2|/f_2\right)\times 100\%$, where f_1 and f_2 are the natural frequencies gained by the experimental and numerical approaches, respectively. The difference of the experimental results relative to the numerical results was less than 4%. Therefore, the vibration properties of the plate could be investigated using the numerical approach.

For the VAT composite plate with amplitude correlation coefficient r=8 mm, the results gained from numerical and experimental methods are listed as well. It can be found that the differences between the experimental results and numerical results are a little larger compared with those of the constant stiffness plate. That may be because the mathematical models used in the current study do not consider the movement of the fiber due to vacuum pressure, on the presumption that all fibers are precisely moved.

The free vibration performances of the VAT composite plates under the considered fiber orientations

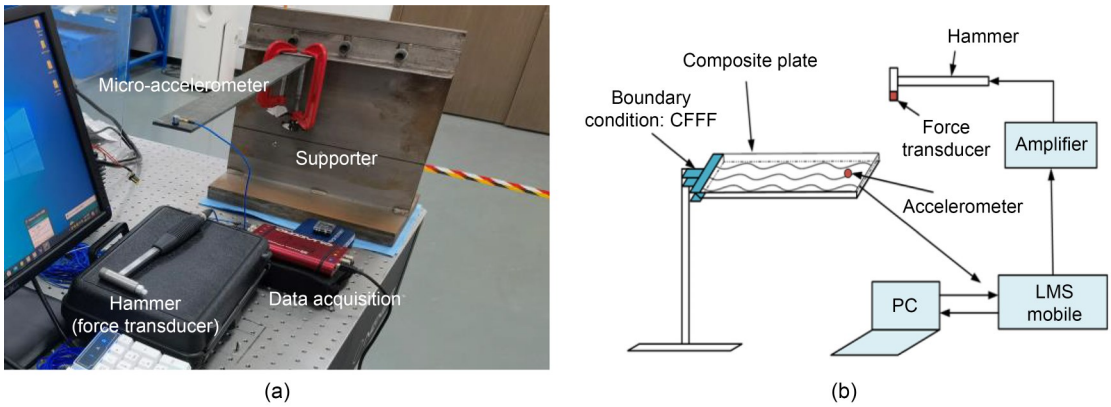

Fig. 2 Installation of vibration test equipment: (a) experimental setup; (b) schematic setup. CFFF stands for boundary condition as clamped on one side when the other three sides are free; LMS stands for learning management system

Table 1 Comparison of the natural frequencies of various composite plates with different fiber functions obtained by experimental and simulation methods

Mode No.	0°			90°			VAT plate (r=8 mm)		
	f_1 (Hz)	f_2 (Hz)	Error (%)	f_1 (Hz)	f_2 (Hz)	Error (%)	f_1 (Hz)	f_2 (Hz)	Error (%)
1	101.8	99.51	2.30	56.4	54.50	3.39	110.0	105.47	4.30
2	280.2	278.81	0.50	126.5	123.50	2.43	312.5	301.64	3.60
3	413.5	400.25	3.31	143.7	139.77	2.81	455.0	432.92	5.10
4	562.3	546.95	2.81	212.3	204.90	3.60	640.0	599.25	6.80

were studied. The non-dimensional natural frequencies $\bar{\omega}_n$ of the structure were established using the formula $\bar{\omega}_n=\omega_{11}L^2\sqrt{\rho/(E_{22}h^2)}$, where ω_{11} is the natural frequencies of the structure, and E_{22} is Young's modulus. All edges were simply supported in the circumstances that are being shown. The parameters for the material were specified as E_{11}=120 GPa, E_{22}=7.9 GPa, E_{12}=5.5 GPa, E_{23}=1.58 GPa, v_{12}=0.33, v_{23}=0.022, and ρ=1580 kg/m^3. The dimensions of the structure are set as L=W=1 m, and h=0.01 m. As for the fiber function, the wave length l is constant as 1 m in this study.

Figs. 3a and 3b reveals the impacts of the amplitude correlation coefficient of the fiber function r on the dimensionless natural frequencies of the VAT composite plates M1 and M2, respectively. The parameter r varies from 0.0 to 0.5 m. The natural frequencies corresponding to the first four modes are displayed and it is revealed that the fiber function has significant impacts on the 2nd, 3rd, and 4th non-dimensional frequencies. Fig. 3a shows that for plate M1, the lowest

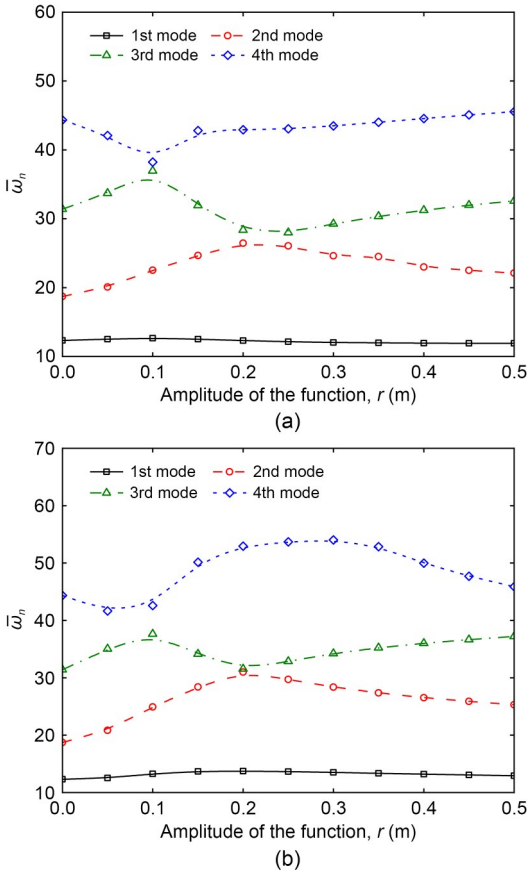

Fig. 3 Effect of fiber function on the natural frequencies of the square VAT laminated composite plates with configurations M1 (a) and M2 (b)

value of the 1st dimensionless natural frequency at 11.90 appears when r=0.5 m. The peak of the 2nd frequency at 26.45 is around the centre of the line, and the value is close to the minimum value in the 3rd frequency. When the parameter r is increased, the 4th natural frequency firstly reduces to its lowest value at 38.23 when r=0.1 m, then it increases. Fig. 3b shows the natural frequencies of plate M2, whose fiber layers vary along its thickness, and more significant variations in the natural frequencies are found due to the change in the fiber function compared with those in M1. This time the minimum value for the 1st natural frequency appears when r=0 m. For the 2nd frequency, when the parameter r=0.2 m, the peak frequency is at 31.00, which is larger than the highest value of the 2nd frequency in Case M1 at 26.45. Besides, the peak of the 3rd frequency in this case at 37.62 is also larger than that in the previous case. Finally, as for the 4th non-dimensional frequency, when the parameter r=0.3 m, the non-dimensional frequency reaches 54.03, which is the largest value in this line. Thus, it can be concluded that the design of VAT plate M2 could further increase the natural frequency.

5.2 Vibration suppression by VAT design

Here, we considered a point force $\tilde{f}_e$ of 10 N that was applied at the centre of the lower left quarter of the plate, with a non-dimensional frequency $\bar{\omega}$ varying in the range of 10 to 35. The damping ratio was set as 0.01. Then the displacement responses at the stimulation point w, the kinetic energy of the whole plate K_p, and the energy transmission path (ETP) were obtained. The effect of the amplitude correlation coefficient of shape parameter r was investigated. An analytical method was also applied to determine the vibration response of the plate with constant stiffness, and the result was compared with the results of the VAT plate with r=0 m using the numerical method. The lines and square symbols represent the numerical and analytical results, respectively.

5.2.1 Forced vibration of configuration M1

Figs. 4a and 4b show the effects of the amplitude correlation coefficient of the fiber function r on w and K_p of the plate M1, respectively. The figures demonstrate good agreement between the analytical and FEM findings. Five cases were investigated with various r of the fiber function, set as 0, 0.05, 0.125, 0.25, and

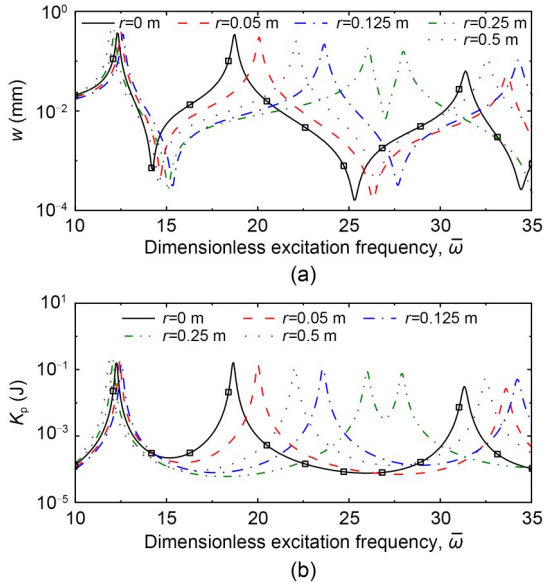

Fig. 4 Effect of fiber function on the displacement (a) and kinetic energy (b) responses of square VAT laminated composite plates with configuration M1

0.5 m for Cases 1, 2, 3, 4, and 5, respectively. Fig. 4a reveals that for the displacement response, when $\bar{\omega}$ is changed, the displacements of the plates with various r are very different. Each first peak in these five cases appears when $\bar{\omega}$ is in the range of 11.5 to 12.5. The first peak in Case 4 with r=0.25 m is the highest among all the instances with a value of 0.41 mm, while the first peak of Case 3 with r=0.125 m appears latest when the dimensionless excitation frequency reaches around 12.64. As for the second peaks in these cases, their corresponding non-dimensional excitation frequencies are very different. For Case 4 with r=0.25 m, the gap between the first and second peaks is the largest, and the second peak appears at $\bar{\omega}$=26.05, while for Case 1 with r=0 m, it appears when $\bar{\omega}$=18.75. Fig. 4b shows that for the M1 configuration, the highest kinetic energy at 0.16646 J is found in Case 1 with r=0 m when $\bar{\omega}$=18.68. For the second peak, the energy response of Case 5 with r=0.5 m is similar to that of Case 2 with r=0.05 m, while the excitation frequency of Case 1 with r=0.05 m is lower. Furthermore, when the amplitude r of the fiber function rises from 0.05 to 0.25 m, the value of the second peak decreases, and the gap between the first two peaks becomes larger.

Fig. 5 shows the energy transmission paths and the dominant mode shape within the square composite plates with configuration M1 for fiber shape r=0.25 m. Three cases were considered and the non-dimensional excitation frequencies were selected as 26.06, 27.99, and 43.06, which are respectively the 2nd, 3rd, and 4th resonant frequencies of the plate. The figure reveals that the vibration energy transmission paths are highly influenced by the stimulating frequencies. Fig. 5a shows

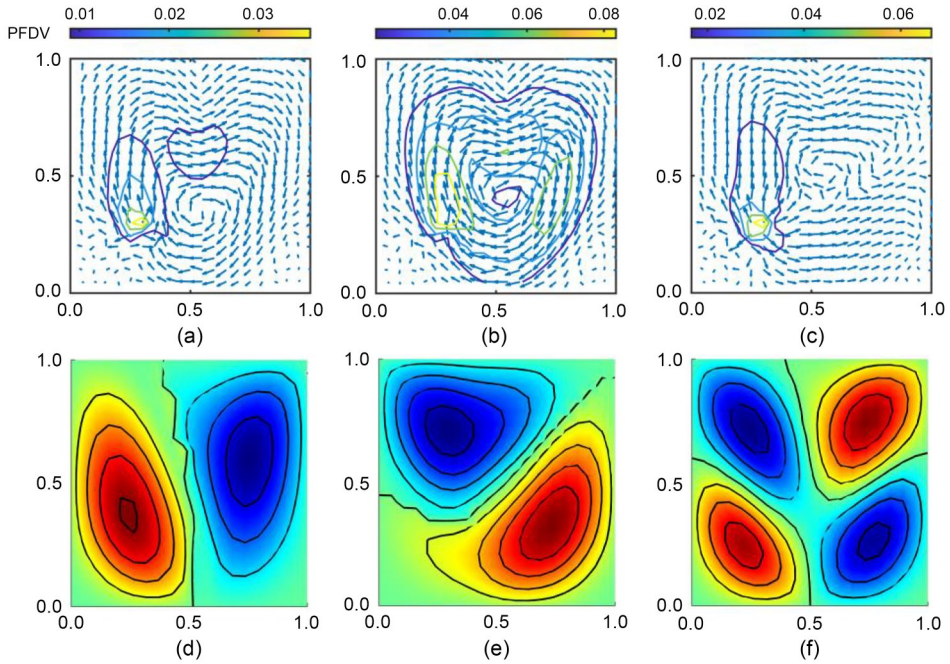

Fig. 5 Energy transmission paths with $\bar{\omega}$=26.06 (a), $\bar{\omega}$=27.99 (b), and $\bar{\omega}$=43.06 (c) and the second (d), the third (e), and the fourth (f) mode shapes within square VAT composite plates under M1 configuration with fiber shape r=0.25 m

that when $\bar{\omega}$=26.06, energy imported from the excitation point mainly flows upwards. In the upper middle half of the plate, the energy first flows to the lower right corner and then to the upper right corner. Afterwards, in the right-hand side (RHS) of the plate, all the energy flows downwards, and the contour line in Fig. 5a becomes heart-shaped. Fig. 5d shows its corresponding dominant mode shape: there are two bending wave forms with one curved nodal line. Moreover, it can be seen from Figs. 5a and 5d that the directions of PFDVs on the nodal line are roughly perpendicular to the nodal lines. The energy transmission paths in M1 when it is activated at the third resonance frequency and its associated dominant mode shape are presented in Figs. 5b and 5e, respectively. Fig. 5b shows that the transmission pattern of the energy is similar to that in Fig. 5a, while the response level is higher here. Besides, Fig. 5e demonstrates four wave forms with a curved nodal line and the PFDVs on the nodal line point to the upper right and lower left corners, which are almost perpendicular to the nodal line. The vibration responses of M1 excited at its fourth resonance frequency are shown in Figs. 5c and 5f. Fig. 5c reveals that in the LHS of the structure, some energy input from the excitation point flows upwards and then to the right, and some energy flows downwards firstly and then also to the right. Besides, a sink is found near the top right corner of the plate. In general, the energy transmission path is similar to a square. On the other hand, Fig. 5f shows four wave forms in the plate, which are located at four corners of the plate, and the contour lines are all broadly oval in shape.

Fig. 6 shows the ETPs and the corresponding dominant mode shapes within the square composite plates under M1 configuration and different fiber parameters, r, which are set as 0.05, 0.25, and 0.50 m for Cases 1, 2, and 3, respectively. The excitation frequency, $\bar{\omega}$=20.07, was selected for three cases, where significant variations in the K_p were found in Fig. 4b. The external force evidently feeds a significant amount of energy into the plate. Under the same stress condition, the responses of the plate are significantly different because of the change in fiber function. Fig. 6a reveals that for Case 1 with r=0.05 m, whose fiber orientation is near 0°, the vibration energy is input from the excitation point. Around the excitation point, the main energy flows to the upper right corner, and some energy flows to the upper left corner. Furthermore, in the upper half of the plate, all the energy flows upwards vertically and then converges to a sink found at the midpoint of the upper edge. In addition, the matching dominant mode shape is shown in Fig. 6d, which demonstrates that there are two wave forms in total, with two bending waves in the direction of OY and one

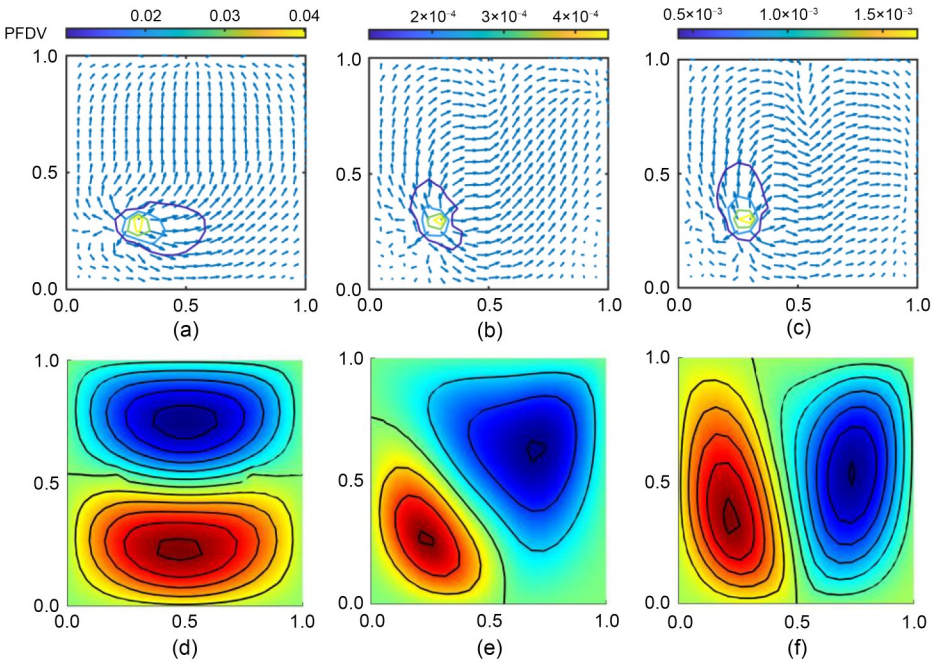

Fig. 6 Energy transmission paths with different fiber shapes r=0.05 m (a), r=0.25 m (b), and r=0.5 m (c) and the corresponding second mode shapes (d)–(f) within square VAT composite plates under configuration M1 excited at $\bar{\omega}$=20.07

bending wave in the direction of *OX*. There is also a curved nodal line found near the centre of the structure. According to Figs. 6a and 6d, it is clear that the PFDVs on the nodal line are pointing straight upwards, perpendicular to the nodal line. Fig. 6b demonstrates the ETPs within the plate under M1 configuration when r=0.25 m. It is revealed that in the LHS of the plate, the vibration energy mainly first flows upwards and then flows to the right. In contrast, in the RHS of the plate, the energy flows to the upper right corner and to the sink generated at the upper half of the right edge. Fig. 6e presents its corresponding dominant mode shape, and it is evident that there are two wave forms in the diagonal corners and a curved nodal line. The ETPs within the plate with r=0.5 m and the dominant mode shapes are presented in Figs. 6c and 6f, respectively. Based on Fig. 6c, it is found that in the LHS of the plate, the energy transmission pattern is similar to that in Fig. 6b, while in the RHS, the energy mainly flows to the right and converges to a sink around the point (1.00 m, 0.25 m). Two wave forms with two bending waves in the *OX* direction can be seen in the structure in Fig. 6f. Besides, a curved nodal line is found, and the PFDVs on this line point to the right, roughly perpendicular to the nodal line.

5.2.2 Forced vibration of configuration M2

Figs. 7a and 7b reveal the impacts of amplitude correlation coefficient r of the fiber function on the w and K_p of the VAT plate M2, respectively. Five cases were investigated with different r values, including 0, 0.05, 0.125, 0.25, and 0.5 m for Cases 1–5, respectively. The analytical and FE findings exhibit good agreement. Fig. 7a shows the w of plate M2 under various non-dimensional excitation frequencies. Among all the cases, the first peak appears in Case 1 with r=0 m when the non-dimensional excitation frequency $\bar{\omega}$=12.29, and the value there is 0.3658 mm. After comparing the first peak in each case, the highest peak, at 0.371 mm, is found in Case 2 with r=0.05 m, when $\bar{\omega}$=12.57, while in Case 4 with r=0.25 m, the value of its first peak is only 0.314 mm. When r=0.25 m, the gap between the first two peaks is the largest compared with other cases. Fig. 7b depicts the K_p of plate M2. In these five cases, the highest K_p at 0.1822 J is found in Case 5 with r=0.5 m, followed by that in Case 2 with r=0.05 m, when the non-dimensional frequency $\bar{\omega}$=12.50. In addition, as for the first peak in each case, the lowest K_p

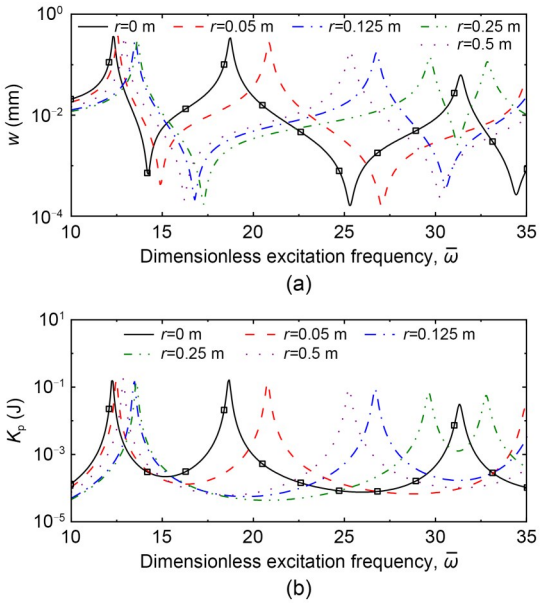

Fig. 7 Effect of the fiber function on the displacement (a) and kinetic energy (b) responses of square VAT laminated composite plates with configuration M2. The lines and square symbols represent the numerical and analytical results, respectively

at 0.1446 J is found in Case 4 with r=0.25 m, when $\bar{\omega}$=13.55. For the second peak, when the amplitude correlation coefficient r of the fiber function increases from 0.05 m to 0.25 m, the value of the second peak decreases, and the gap between the first two peaks is larger. When $\bar{\omega}$ is between 10 and 35, there are only two peaks in all cases except Case 1 with r=0 m and Case 4 with r=0.25 m.

Fig. 8 shows the ETPs and corresponding dominant mode shapes within the composite plates under configuration M2, with the amplitude correlation coefficient of fiber function r=0.25 m. Three cases are studied here with different non-dimensional excitation frequencies; these are chosen as 29.71, 32.87, and 53.68, which are the 2nd, 3rd, and 4th natural frequencies of the structure, respectively. Fig. 8a shows the ETPs within plate M2 excited under the 2nd natural frequency. It is revealed that the main energy import from the excitation point flows upwards and then to the upper right corner. In contrast, in the RHS of the plate, the energy first flows to the lower right corner and then to the lower left corner. Compared with Fig. 5a under M1, the response level here in Fig. 8a is lower, which means that such a plate with configuration M2 can somewhat suppress the vibration. Fig. 8d displays the form of the dominant mode, where the structure

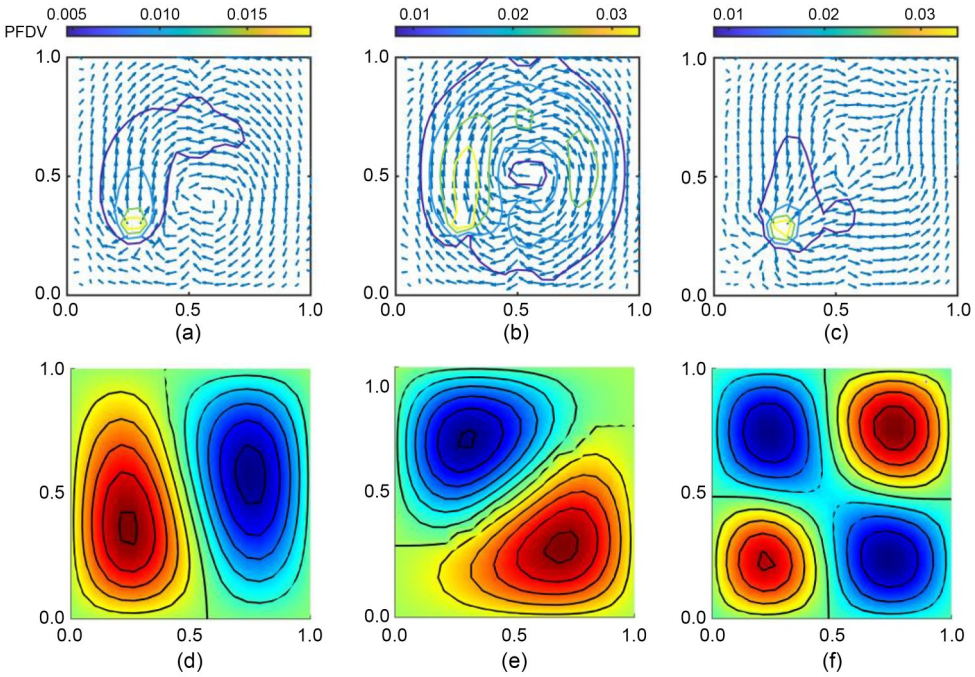

Fig. 8 Energy transmission paths with $\bar{\omega}$=29.71 (a), $\bar{\omega}$=32.87 (b), and $\bar{\omega}$=53.68 (c) and the second (d), the third (e), and the fourth (f) mode shapes within square VAT composite plates under M2 configuration with fiber shape r=0.25 m

has two wave forms. Two bending waves are present in the direction of *OX*, while one is present in the direction of *OY*. Moreover, in areas close to the center of the plate, there is a curved nodal line. Fig. 8b shows the ETPs within the plate, when $\bar{\omega}$=32.87. It can be seen that the transmission pattern of the energy here is similar to that in Fig. 8b, and the contour line is approximately circular. Fig. 8e presents the corresponding dominant mode shape. Four wave forms and a curved nodal line are found in the structure. Based on Figs. 8b and 8e, the PFDVs on the nodal line are approximately perpendicular to the nodal line in their direction. The ETPs within the plate excited at its fourth natural frequency are determined in Fig. 8c. Some vibration energy imported from the excitation point flows upwards vertically and then to the right to a sink located at the top right corner of the structure. On the other hand, some energy flows to the right and then flows upwards. A total of four wave shapes can be seen in Fig. 8f, with two bending in the *OX* direction and two bending in the *OY* direction. Nodal lines are also shown in the figure. The PFDVs on nodal lines point horizontally or vertically, both of which are almost perpendicular to the nodal line. Based on Fig. 8, it can be concluded that the vibrations of ETPs within the plate are affected by the frequency of the excitation sustainably.

Fig. 9 shows the ETPs and the corresponding dominant mode shapes within square composite plates under M2 configuration with different fiber function parameters r of 0.05, 0.25, and 0.50 m. These three plates were all excited at $\bar{\omega}$=20.85, where the large differences in terms of the K_p were found in Fig. 7. Fig. 9a reveals the ETPs within the plate under r=0.05 m, where the vibration energy is imported from the excitation point. Much energy flows to the right and then upwards. Besides, in the upper half of the structure, all the energy flows upwards vertically and then converges to the sink found at the midpoint of the upper edge. As for the corresponding dominant mode shape, Fig. 9d shows two wave forms in the structure with two bending waves in the *OY* direction. A horizontal nodal line is located at the centre of the structure. It is evident that the PFDVs on the nodal line are pointing upward vertically, which is nearly perpendicular to the nodal line. On the other hand, when r=0.25 m, the ETPs within the plate are shown in Fig. 9b. It can be seen that in the LHS of the plate, the main energy first flows to the upper right corner and then to the lower right corner, while in the RHS of the plate, all the energy flows to the upper right corner to a sink that is found near the point (0.9 m, 0.8 m). Fig. 9e shows three wave forms in the plate with a curved nodal line. As for the

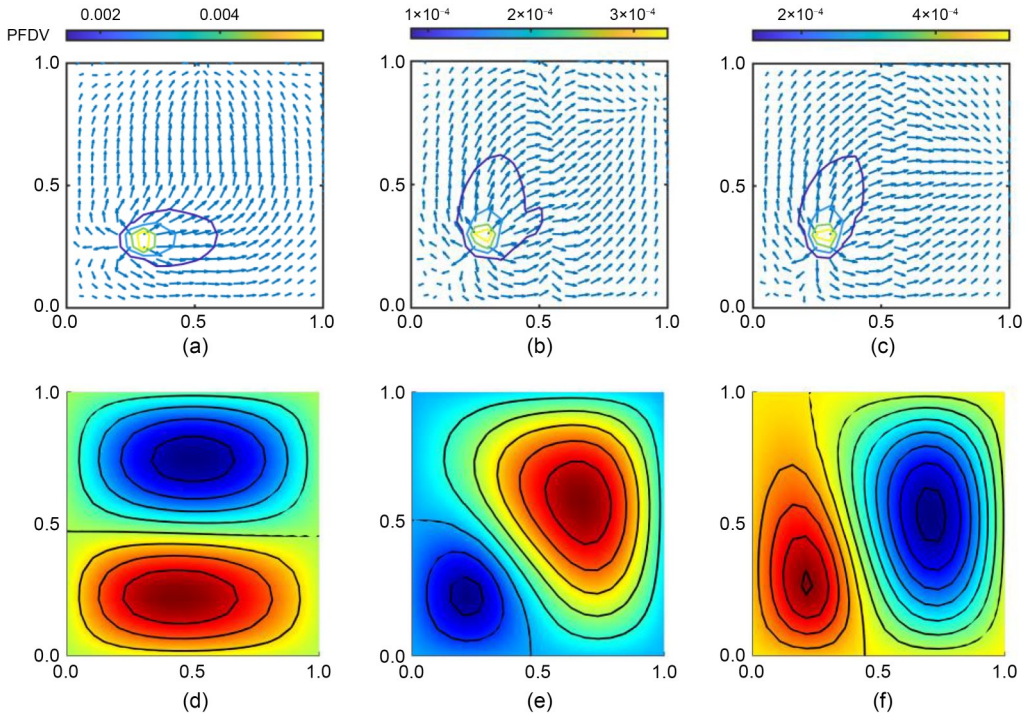

Fig. 9 Energy transmission paths with different fiber shapes r=0.05 m (a), r=0.25 m (b), and r=0.5 m (c) and the corresponding second mode shapes (d)–(f) within square VAT composite plates under M2 configuration excited at $\bar{\omega}$=20.85

plate with r=0.5 m, Fig. 9c reveals that in the LHS of the plate, the transmission pattern of the energy is similar to that in Fig. 8b. In contrast, in the RHS of the plate, the energy firstly flows horizontally to the right, then it converges to the sink that is situated in the centre of the right edge. Fig. 9f displays the dominant mode shape of the plate with r=0.5 m. It is revealed that there are three wave forms and a curved nodal line. Additionally, it is discovered that PFDVs on the nodal line are oriented horizontally to the right and are roughly perpendicular to the nodal line. Based on Fig. 9, it can be concluded that under the same condition of excitation stress, the fiber function has a considerable impact on the responses of the plate.

5.3 Vibration suppression by attaching a passive device

In addition to the change of fiber function, attaching a passive device can also suppress the vibration response of the plate. To this end, the centre of the bottom left quadrant of the plate was subjected to a point force $\tilde{f}_e$ of 10 N, and the non-dimensional frequency of this force $\bar{\omega}$ varied from 5 to 35. The damping ratio was assumed as 0.01. The substructure method was used, and the kinetic energy K_p and the ETPs were both focused on. We studied two different passive devices C1 and C2 installed at the upper right quarter of the plate, and the effect of the nonlinear device was also investigated.

5.3.1 Forced vibration of configuration M0

Fig. 10 shows the effect of coefficients of the spring and damper on the K_p of the constant-stiffness structure M0 with fiber angle θ=0°. The forced response was also calculated using an analytical technique and the outcomes were contrasted with those obtained using

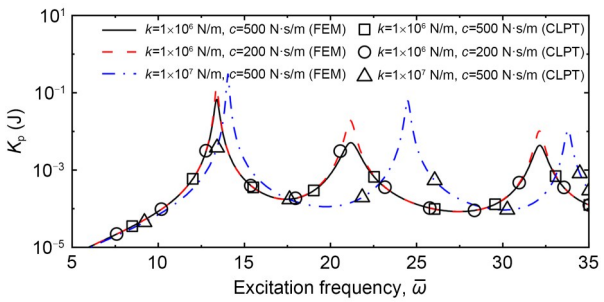

Fig. 10 Effect of the passive device (spring and damper in parallel) on the K_p of the composite plate under M0 configuration, with fiber angle θ=0°, attached to the passive device at point B (0.75 m, 0.75 m). CLPT: classical laminated plate theory

the numerical method. The lines and symbols represent the numerical and analytical results, respectively. Based on the result, good agreements between the analytical and FE results could be found. Fig. 10 reveals that when the coefficient of the passive device is changed, the kinetic response of the plates is also very different. It is shown that among the three cases, the highest peak at 0.3131 J appears in Case 3 with k=1×10^7 N/m and c=500 N·s/m, when $\bar{\omega}$=14.04. As for Case 2 with k=1×10^6 N/m and c=200 N·s/m, the corresponding excitation frequency is similar to that in Case 1, while the level of the kinetic energy is increased to 0.14374 J, which means that the decrease in the coefficient of the damper can increase the response of the structure. The peak of Case 3 with k=1×10^7 N/m and c=500 N·s/m appears the last, due to which the increase of the coefficient of the spring can move the peak to the right.

5.3.2 Forced vibration of configuration M1

Figs. 11 and 12 respectively show the effects of linear and nonlinear passive device C1 on the K_p of the plate under M1 configuration with the amplitude correlation coefficient of the fiber function r=0.25 m. Fig. 11a demonstrates that the spring may substantially impact the kinetic response of the plate. Under c=500 N·s/m and λ=1, it is evident that the peaks of kinetic energy curves are pushed to higher frequencies as the spring stiffness increases. Compared with that in the plate with k=1×10^5 N/m, the non-dimensional resonant frequency in the plate with k=1×10^7 N/m is increased from 9.06 to 14.04. Moreover, a reduced elevation of the kinetic energy of the plate in the low-frequency range with $\bar{\omega}$<8.64 may also result from the stiffness of the attached spring. Fig. 11b shows the effect of the damper; the coefficients of spring and inerter were set as k=1×10^5 N/m and λ=1, respectively. Based on the result, it is evident that increasing the damper c could lower the maximum values of K_p. For example, when the damper c=1000 N·s/m the peak value is only 8.19×10^5 J, which is around 0.9% of that in the plate without the damper. However, it is noted that the impact of damper on the vibration level of the plate will be minimal if the stimulation frequency is not within the resonant areas. Fig. 11c demonstrates the effect of the inerter, with the setting for the spring and damper coefficients at k=1×10^5 N/m and c=500 N·s/m, respectively. The first peaks in the K_p curves move to lower frequencies when the coefficient of the inerter is increased, and the value of the peaks is also reduced. It is also found that when $\bar{\omega}$ is in the range from 10 to 13, the attachment of the inerter can decrease the

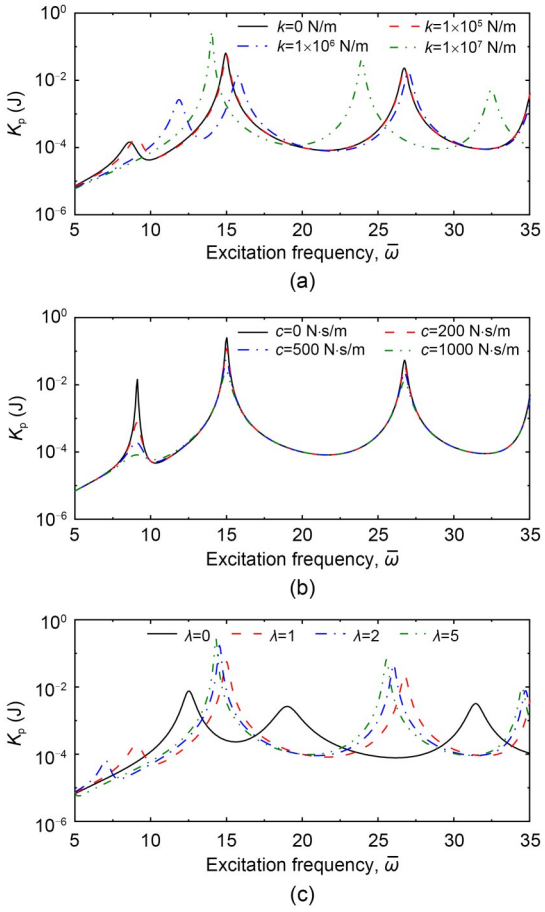

Fig. 11 Effect of passive device C1 (in-parallel) on the K_p of VAT plate under M1 configuration with fiber function r=0.25 m, attached to the passive device at point B (0.75 m, 0.75 m): (a) c=1000 N·s/m, λ=0.3; (b) k=1×10^5 N/m, λ=0.3; (c) k=1×10^5 N/m, c=1000 N·s/m

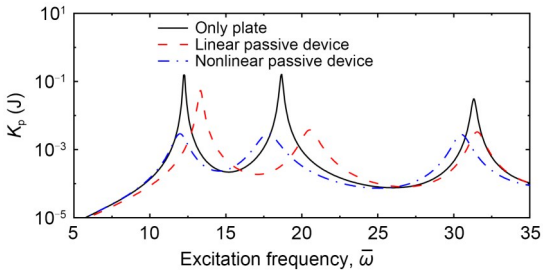

Fig. 12 Effect of linear and nonlinear inerter-based passive device C1 (in-parallel) on the K_p of VAT plate under M1 configuration, attached to the passive device at point B (0.75 m, 0.75 m). The parameters are set as r=0.25 m, k=5×10^6 N/m, c=500 N·s/m, and λ=0.5

responses. Fig. 12 shows the effect of the nonlinear passive device C1 on the plate, with the coefficients of the devices set as k=1×10^6 N/m, c=500 N·s/m, and λ=0.1. It is revealed that attaching the nonlinear device decreases the resonant frequency compared with the plate without the passive device. Among these three cases, the value of the first peak in the case with the nonlinear device is the lowest at 0.00292 J.

Figs. 13 and 14 respectively illustrate the effects of linear and nonlinear passive device C2 on the K_p response of the plate M1 with r=0.25 m. Various coefficients of the spring, damper, and inerter were studied. Under c=1000 N·s/m and λ=0.3, Fig. 13a shows that changing the spring stiffness can significantly influence the kinetic response of the plates and, when the spring is installed, one more peak appears when $\bar{\omega}$ is in the range of 10 to 17. It is clear that among the first peaks in each case, the lowest value at 0.00041 J appears for the plate with k=1×10^5 N/m, when the non-dimensional excitation frequency $\bar{\omega}$=10.32. Besides, with the stiffness of the spring rising from 5×10^5 to 5×10^6 N/m, the corresponding non-dimensional frequencies of the second peaks of these cases are larger, and the values of these peaks become higher. On the other hand, the effect of the damper is seen in Fig. 13b, and the coefficients of the other two elements are set as k=10^5 N/m and λ=0.3. It is found that the first peaks of all studied examples decrease as the damping coefficient increases. To be specific, compared with that for the plate without the damper, the damper with c= 400 N·s/m can reduce the peak value from 0.0345 to 0.0045 J. Such evident decline is also found in the second peak region. Fig. 13c demonstrates the effect of the inerter, and the settings for the spring and damper coefficients are k=1×10^5 N/m and c=1000 N·s/m, respectively. Similar to the damper, the differences caused by various inerters here are mainly reflected in the response value, rather than the resonance frequencies. With the increase in the coefficient of the inerter from 0.1 to 0.3, the first peak in each case shifts right to the higher frequencies, and the value of peaks is reduced. As for the second peak in all cases, the corresponding dimensionless frequency of Case 4 with λ=0.4 is the highest at 18.40. Fig. 14 shows the effect of the nonlinear passive device C2 on the plate, with the coefficients of the devices set as k=5×10^6 N/m, c=500 N·s/m, and λ=0.5. It is revealed that among the three cases studied here, the value of the first peak in the case with the nonlinear device is the lowest at 0.0136 J. At the same time, attaching the nonlinear passive device would decrease the corresponding dimensionless frequency of the first peak when compared with a plate without the device.

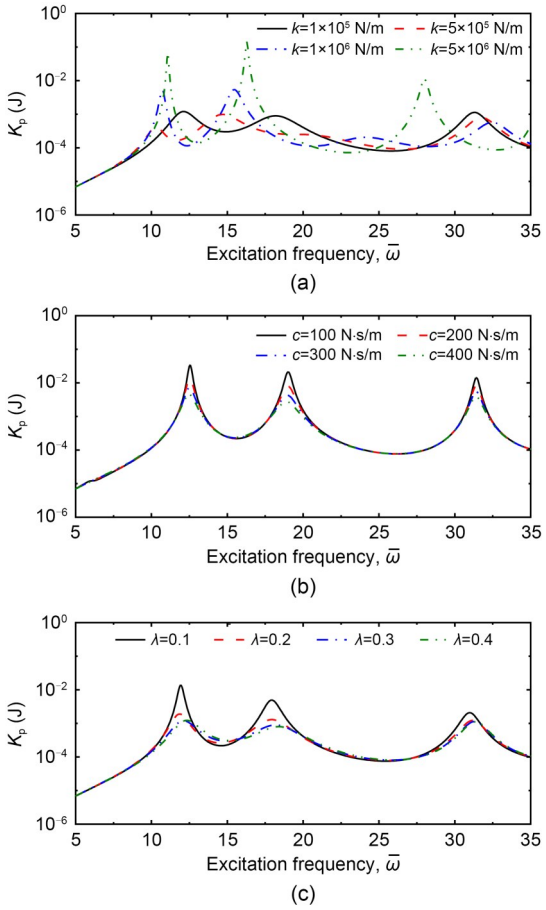

Fig. 13 Effect of passive device C2 (in-series) on the K_p value of VAT plate under M1 configuration with fiber function r=0.25 m, attached to the passive device at point B (0.75 m, 0.75 m): (a) c=1000 N·s/m, λ=0.3; (b) k=1×10^5 N/m, λ=0.3; (c) k=1×10^5 N/m, c=1000 N·s/m

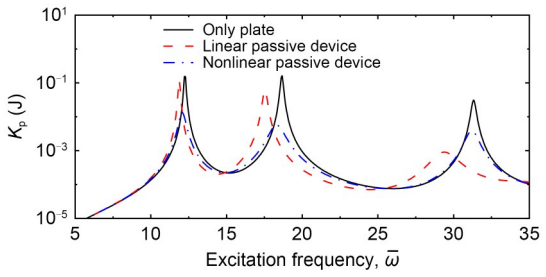

Fig. 14 Effect of linear and nonlinear inerter-based passive device C2 (in-series) on the K_p value of VAT plate under M1 configuration, attached to the passive device at point B (0.75 m, 0.75 m). The parameters are set as r=0.25 m, k= 5×10^6 N/m, c=500 N·s/m, and λ=0.5

6 Conclusions

This paper investigated the vibration properties of composite plates with variable stiffness laminated with passive devices. First, the substructure methods based on the numerical FE and analytical approaches were developed. In this method, the whole FE of the entire structure is not necessary, and the results may be easily obtained by changing the parameters of the receptance function, which lowers the computing costs. Using the substructure-based PFA method, the vibration performances can be quantified. Then, the natural frequencies of structures were determined and the displacement, kinetic energy responses and energy transmission paths were also analyzed using the PFA method. The influences of fiber scheme and various passive devices on the vibration performances of the structure were examined. The above techniques can aid in improving our understanding of the vibration characteristics of composite structures, allowing for the design of structures that perform better at vibration suppression.

In this work, two kinds of VAT composites with different fiber shape schemes were investigated for their vibration properties. The natural frequencies of the composite plate were shown to be significantly impacted by the fiber function. We examined the effect of the fiber function on the displacement and energy responses of the VAT plate and found that the fiber function could change the value of response peaks and the corresponding non-dimensional excitation frequencies. Furthermore, ETPs and the dominant mode shapes within the structure with two various fiber schemes were drawn. The main ETPs correlated well with the dominant mode shape. It was demonstrated that the ETPs and mode shapes were altered to a large extent by adjusting the fiber layer scheme of the plate. The results illustrated the capability of adjusting the fiber function of VAT plates to raise their vibration suppression levels.

Subsequently, the effects on the forced vibration response from adding various inerter-based passive devices were studied. The spring, damper, and inerter elements were used in combination to build the inerter-based passive devices, and both linear and nonlinear springs were considered. With the devices applied, the peak value and the corresponding frequencies were changed significantly, showing advantages for vibration suppression. When the inerter was connected in parallel or series with the spring and damper, the two alternative configurations did not function similarly. By varying the coefficients of the device, the effect of each element was better understood. Besides, compared with a passive device containing the linear spring, the vibration suppression ability of the device with a nonlinear spring was much stronger in terms of the peak value. Overall, the findings demonstrated that after composite laminates had been designed and manufactured, their vibration suppression performance could be enhanced further by attaching passive devices.

Acknowledgments

This work is supported by the National Natural Science Foundation of China (Nos. 12172185, U1809218, and U1864211), the Zhejiang Provincial Natural Science Foundation of China (Nos. LY22A020006, LD22E050011, and LQ23A020003), the Ningbo Municipal Natural Science Foundation of China (No. 2022J174), and the Ningbo Key Projects of Science and Technology Innovation 2025 Plan (No. 2021Z124).

Author contributions

Jian YANG designed the research. Chen ZHOU processed the corresponding data. Chen ZHOU wrote the first draft of the manuscript. Jian YANG and Chendi ZHU helped to organize the manuscript. Jian YANG and Yingdan ZHU revised and edited the final version.

Conflict of interest

Chen ZHOU, Jian YANG, Yingdan ZHU, and Chendi ZHU declare that they have no conflict of interest.

References

Abdalla MM, Setoodeh S, Gürdal Z, 2007. Design of variable stiffness composite panels for maximum fundamental frequency using lamination parameters. *Composite Structures*, 81(2):283-291. https://doi.org/10.1016/j.compstruct.2006.08.018

Akbarzadeh AH, Nik MA, Pasini D, 2016. Vibration responses and suppression of variable stiffness laminates with optimally steered fibers and magnetostrictive layers. *Composites Part B: Engineering*, 91:315-326. https://doi.org/10.1016/j.compositesb.2016.02.003

Blom AW, Setoodeh S, Hol JMAM, et al., 2008. Design of variable-stiffness conical shells for maximum fundamental eigenfrequency. *Computers & Structures*, 86(9):870-878. https://doi.org/10.1016/j.compstruc.2007.04.020

Chen HY, Mao XY, Ding H, et al., 2020. Elimination of multi-mode resonances of composite plate by inertial nonlinear energy sinks. *Mechanical Systems and Signal Processing*, 135:106383. https://doi.org/10.1016/j.ymssp.2019.106383

Cho DS, Kim BH, Kim JH, et al., 2015. Forced vibration analysis of arbitrarily constrained rectangular plates and stiffened panels using the assumed mode method. *Thin-Walled Structures*, 90:182-190. https://doi.org/10.1016/j.tws.2015.01.020

Coburn BH, Wu ZM, Weaver PM, 2014. Buckling analysis of stiffened variable angle tow panels. *Composite Structures*, 111:259-270. https://doi.org/10.1016/j.compstruct.2013.12.029

Dai W, Yang J, Shi BY, 2020. Vibration transmission and power flow in impact oscillators with linear and nonlinear constraints. *International Journal of Mechanical Sciences*, 168:105234. https://doi.org/10.1016/j.ijmecsci.2019.105234

Dai W, Yang J, Wiercigroch M, 2022. Vibration energy flow transmission in systems with Coulomb friction. *International Journal of Mechanical Sciences*, 214:106932. https://doi.org/10.1016/j.ijmecsci.2021.106932

Gurdal Z, Olmedo R, 1993. In-plane response of laminates with spatially varying fiber orientations-variable stiffness concept. *AIAA Journal*, 31(4):751-758. https://doi.org/10.2514/3.11613

Honda S, Oonishi Y, Narita Y, et al., 2008. Vibration analysis of composite rectangular plates reinforced along curved lines. *Journal of System Design and Dynamics*, 2(1):76-86. https://doi.org/10.1299/jsdd.2.76

Houmat A, 2013. Nonlinear free vibration of laminated composite rectangular plates with curvilinear fibers. *Composite Structures*, 106:211-224. https://doi.org/10.1016/j.compstruct.2013.05.058

Ibrahim RA, 2008. Recent advances in nonlinear passive vibration isolators. *Journal of Sound and Vibration*, 314(3-5):371-452. https://doi.org/10.1016/j.jsv.2008.01.014

Jahangir I, Barazanchy D, van Zanten FJ, et al., 2022. Tow path planning strategies for fiber steered laminates. *Journal of Aircraft*, 59(2):502-514. https://doi.org/10.2514/1.C036481

Javidialesaadi A, Wierschem NE, 2019. An inerter-enhanced nonlinear energy sink. *Mechanical Systems and Signal Processing*, 129:449-454. https://doi.org/10.1016/j.ymssp.2019.04.047

Jiang JZ, Matamoros-Sanchez AZ, Goodall RM, et al., 2012. Passive suspensions incorporating inerters for railway vehicles. *Vehicle System Dynamics*, 50(Supplement):263-276. https://doi.org/10.1080/00423114.2012.665166

Lazar IF, Neild SA, Wagg DJ, 2014. Using an inerter-based device for structural vibration suppression. *Earthquake Engineering & Structural Dynamics*, 43(8):1129-1147. https://doi.org/10.1002/eqe.2390

Li Y, Jiang JZ, Neild S, 2017. Inerter-based configurations for main-landing-gear shimmy suppression. *Journal of Aircraft*, 54(2):684-693. https://doi.org/10.2514/1.C033964

Lopes CS, Camanho PP, Gürdal Z, et al., 2007. Progressive failure analysis of tow-placed, variable-stiffness composite panels. *International Journal of Solids and Structures*, 44(25-26):8493-8516. https://doi.org/10.1016/j.ijsolstr.2007.06.029

Mace BR, Shorter PJ, 2000. Energy flow models from finite element analysis. *Journal of Sound and Vibration*, 233(3):369-389. https://doi.org/10.1006/jsvi.1999.2812

Nik MA, Fayazbakhsh K, Pasini D, et al., 2014a. Optimization of variable stiffness composites with embedded defects induced by automated fiber placement. *Composite Structures*, 107:160-166. https://doi.org/10.1016/j.compstruct.2013.07.059

Nik MA, Fayazbakhsh K, Pasini D, et al., 2014b. A comparative study of metamodeling methods for the design optimization of variable stiffness composites. *Composite Structures*, 107:494-501. https://doi.org/10.1016/j.compstruct.2013.08.023

Pedersen P, 1991. On thickness and orientational design with orthotropic materials. *Structural Optimization*, 3(2):69-78. https://doi.org/10.1007/BF01743275

Rahman T, Ijsselmuiden ST, Abdalla MM, et al., 2011. Postbuckling analysis of variable stiffness composite plates using a finite element-based perturbation method. *International Journal of Structural Stability and Dynamics*, 11(4):735-753. https://doi.org/10.1142/S0219455411004324

Raju G, Wu ZM, Weaver PM, 2015. Buckling and postbuckling of variable angle tow composite plates under in-plane shear loading. *International Journal of Solids and Structures*, 58:270-287. https://doi.org/10.1016/j.ijsolstr.2015.01.011

Reddy JN, 1997. Mechanics of Laminated Composite Plates: Theory and Analysis. CRC Press, Boca Raton, USA.

Rivin EI, 2003. Passive Vibration Isolation. ASME Press, New York, USA.

Setoodeh S, Abdalla MM, Gürdal Z, 2005. Combined topology and fiber path design of composite layers using cellular automata. *Structural and Multidisciplinary Optimization*, 30(6):413-421. https://doi.org/10.1007/s00158-005-0528-y

Shi BY, Yang J, 2020. Quantification of vibration force and power flow transmission between coupled nonlinear oscillators. *International Journal of Dynamics and Control*, 8(2):

418-435.
https://doi.org/10.1007/s40435-019-00560-7

Shi BY, Yang J, Rudd C, 2019. On vibration transmission in oscillating systems incorporating bilinear stiffness and damping elements. *International Journal of Mechanical Sciences*, 150:458-470.
https://doi.org/10.1016/j.ijmecsci.2018.10.031

Smith MC, Wang FC, 2004. Performance benefits in passive vehicle suspensions employing inerters. *Vehicle System Dynamics*, 42(4):235-257.
https://doi.org/10.1080/00423110412331289871

Tan P, Nie GJ, 2016. Free and forced vibration of variable stiffness composite annular thin plates with elastically restrained edges. *Composite Structures*, 149:398-407.
https://doi.org/10.1016/j.compstruct.2016.04.021

Vijayachandran AA, Waas AM, 2022a. Minimizing stress concentrations using steered fiberpaths and incorporating realistic manufacturing signatures. *International Journal of Non-Linear Mechanics*, 146:104160.
https://doi.org/10.1016/j.ijnonlinmec.2022.104160

Vijayachandran AA, Waas AM, 2022b. Steered fiber paths for improved in-plane compressive response of aerostructural panels: experimental studies and numerical modeling. *Composite Structures*, 289:115426.
https://doi.org/10.1016/j.compstruct.2022.115426

Wang FC, Liao MK, Liao BH, et al., 2009. The performance improvements of train suspension systems with mechanical networks employing inerters. *Vehicle System Dynamics*, 47(7):805-830.
https://doi.org/10.1080/00423110802385951

Wang FC, Hong MF, Chen CW, 2010. Building suspensions with inerters. *Proceedings of the Institution of Mechanical Engineers, Part C: Journal of Mechanical Engineering Science*, 224(8):1605-1616.
https://doi.org/10.1243/09544062JMES1909

Wang ZH, Xing JT, Price WG, 2002. Power flow analysis of indeterminate rod/beam systems using a substructure method. *Journal of Sound and Vibration*, 249(1):3-22.
https://doi.org/10.1006/jsvi.2001.3645

White SC, Raju G, Weaver PM, 2014. Initial post-buckling of variable-stiffness curved panels. *Journal of the Mechanics and Physics of Solids*, 71:132-155.
https://doi.org/10.1016/j.jmps.2014.07.003

White SC, Weaver PM, Wu KC, 2015. Post-buckling analyses of variable-stiffness composite cylinders in axial compression. *Composite Structures*, 123:190-203.
https://doi.org/10.1016/j.compstruct.2014.12.013

Wu CP, Lee CY, 2001. Differential quadrature solution for the free vibration analysis of laminated conical shells with variable stiffness. *International Journal of Mechanical Sciences*, 43(8):1853-1869.
https://doi.org/10.1016/S0020-7403(01)00010-8

Wu ZM, Weaver PM, Raju G, et al., 2012. Buckling analysis and optimisation of variable angle tow composite plates. *Thin-Walled Structures*, 60:163-172.
https://doi.org/10.1016/j.tws.2012.07.008

Wu ZM, Raju G, Weaver PM, 2013. Postbuckling analysis of variable angle tow composite plates. *International Journal of Solids and Structures*, 50(10):1770-1780.
https://doi.org/10.1016/j.ijsolstr.2013.02.001

Wu ZM, Raju G, Weaver PM, 2018. Optimization of post-buckling behaviour of variable thickness composite panels with variable angle tows: towards "Buckle-Free" design concept. *International Journal of Solids and Structures*, 132-133:66-79.
https://doi.org/10.1016/j.ijsolstr.2017.08.037

Xiong YP, Xing JT, Price WG, 2001. Power flow analysis of complex coupled systems by progressive approaches. *Journal of Sound and Vibration*, 239(2):275-295.
https://doi.org/10.1006/jsvi.2000.3159

Xiong YP, Xing JT, Price WG, 2003. A general linear mathematical model of power flow analysis and control for integrated structure-control systems. *Journal of Sound and Vibration*, 267(2):301-334.
https://doi.org/10.1016/S0022-460X(03)00194-9

Yang J, Xiong YP, Xing JT, 2013. Dynamics and power flow behaviour of a nonlinear vibration isolation system with a negative stiffness mechanism. *Journal of Sound and Vibration*, 332(1):167-183.
https://doi.org/10.1016/j.jsv.2012.08.010

Yang J, Xiong YP, Xing JT, 2014. Nonlinear power flow analysis of the Duffing oscillator. *Mechanical Systems and Signal Processing*, 45(2):563-578.
https://doi.org/10.1016/j.ymssp.2013.11.004

Yang J, Xiong YP, Xing JT, 2015. Power flow behaviour and dynamic performance of a nonlinear vibration absorber coupled to a nonlinear oscillator. *Nonlinear Dynamics*, 80(3):1063-1079.
https://doi.org/10.1007/s11071-014-1556-1

Yang J, Xiong YP, Xing JT, 2016. Vibration power flow and force transmission behaviour of a nonlinear isolator mounted on a nonlinear base. *International Journal of Mechanical Sciences*, 115-116:238-252.
https://doi.org/10.1016/j.ijmecsci.2016.06.023

Zhang SY, Jiang JZ, Neild S, 2017. Optimal configurations for a linear vibration suppression device in a multi-storey building. *Structural Control and Health Monitoring*, 24(3):e1887.
https://doi.org/10.1002/stc.1887

Zhu CD, Yang J, 2019. Free and forced vibration analysis of composite laminated plates. Proceedings of the 26th

International Congress on Sound and Vibration.

Zhu CD, Yang J, 2022. Vibration transmission and energy flow analysis of variable stiffness laminated composite plates. *Thin-Walled Structures*, 180:109927. https://doi.org/10.1016/j.tws.2022.109927

Zhu CD, Yang J, Rudd C, 2021a. Vibration transmission and energy flow analysis of L-shaped laminated composite structure based on a substructure method. *Thin-Walled Structures*, 169:108375. https://doi.org/10.1016/j.tws.2021.108375

Zhu CD, Yang J, Rudd C, 2021b. Vibration transmission and power flow of laminated composite plates with inerter-based suppression configurations. *International Journal of Mechanical Sciences*, 190:106012. https://doi.org/10.1016/j.ijmecsci.2020.106012

Zuo H, Yang ZB, Chen XF, et al., 2015. Analysis of laminated composite plates using wavelet finite element method and higher-order plate theory. *Composite Structures*, 131: 248-258. https://doi.org/10.1016/j.compstruct.2015.04.064